








Spin-singlet to triplet Cooper pair converter interface

Matthew Rogers ^{1✉}, Alistair Walton¹, Machiel G. Flokstra², Fatma Al Ma'Mari³, Rhea Stewart², Stephen L. Lee², Thomas Prokscha ⁴, Andrew J. Caruana ⁵, Christian J. Kinane⁵, Sean Langridge ⁵, Harry Bradshaw ⁶, Timothy Moorsom¹, Mannan Ali¹, Gavin Burnell ¹, Bryan J. Hickey¹ & Oscar Cespedes ^{1✉}

Combining magnetic and superconducting functionalities enables lower energy spin transfer and magnetic switching in quantum computing and information storage, owing to the dissipationless nature of quasi-particle mediated supercurrents. Here, we put forward a system where emergent spin-ordering and diffusion of Cooper pairs are achieved at a non-intrinsically magnetic nor superconducting metallo-molecular interface. Electron transport, magnetometry and low-energy muon spin rotation are used to probe time-reversal symmetry breaking in these structures. By comparing the Meissner expulsion in a system including a Cu/C₆₀ spin-converter interface to one without, we observe a paramagnetic contribution that can be explained due to the conversion of spin-singlet Cooper pair states into odd-frequency triplet states. These results demonstrate the potential of metallo-molecular interfaces to achieve singlet to triplet Cooper pair conversion, a capability not present in either metal or molecule separately that could be used in the generation and controlled diffusion of spin polarised dissipationless currents.

¹School of Physics and Astronomy, University of Leeds, Leeds, UK. ²School of Physics and Astronomy, SUPA, University of St Andrews, St Andrews, UK. ³Department of Physics, Sultan Qaboos University, Muscat, Oman. ⁴Laboratory for Muon Spin Spectroscopy, Paul Scherrer Institute, Villigen, Switzerland. ⁵ISIS Neutron and Muon Source, Rutherford Appleton Laboratory, STFC, Didcot, UK. ⁶Department of Materials Science and Metallurgy, University of Cambridge, Cambridge, UK. ✉email: M.D.Rogers@leeds.ac.uk; o.cespedes@leeds.ac.uk

According to conventional theories on the superconducting condensate, ferromagnetism and superconductivity are antagonistic states of matter. This is due to the ferromagnetic exchange field imparting a pair-breaking effect upon conventional spin-singlet superconducting pair correlations that possess opposing spin -i.e. spin up/down electron pairs. However, local magnetic order emergent at metallo-molecular multilayers can be combined with superconducting proximity effects to generate a region where both magnetic exchange and superconducting pair diffusion are present. Organic superconducting molecules and ferromagnetic metal complexes have been used to chemically design materials where superconductivity and magnetism are shown to coexist¹. The spin dynamics of molecular magnets are heavily influenced by the superconducting order of a lead substrate². Evidence of equal-spin triplet-pairing p-wave symmetry in proximity systems, which feature adsorbed helical chiral molecules, shows the potential of molecular structures in manipulating the symmetry of pair correlations^{3,4}. The realisation of super-spintronic devices requires the coalescence of both superconducting and ferromagnetic long-range order in a single system. Despite this, the theoretical prediction of odd-frequency spin-triplet pair states, with even spin parity, arising through the design of superconductor/ferromagnetic, allows for complete synergy between superconductivity and spintronics^{5–9}.

Odd-frequency superconducting correlations have been probed successfully using transport measurements^{10,11}, tunnelling spectroscopy¹² and low-energy muon spin rotation (LE- μ SR). The latter directly probes the paramagnetic Meissner screening generated by odd-frequency spin-triplet Cooper pairs^{13–15}. Typical super-spintronic devices require the generation of a $S_z = \pm 1$ long-

range spin-triplet component (LRTC) to preserve the superconducting correlations inside ferromagnetic layers^{16,17}. Unlike spin-singlet and $S_z = 0$ spin-triplet pairs, the equal-spin pairing of the long-range spin-triplet component is no longer subject to pair-breaking mechanisms within ferromagnetic layers. These correlations are thus able to carry dissipationless spin information while facilitating the superconducting proximity of ferromagnets owing to their extended propagation length in spin-polarised materials.

For applications and research pathways into low power electronics and quantum computing, there are two drawbacks. Firstly, the need to grow complex compounds or magnetic materials with superconductors, which can have a significant impact, e.g. on the information coherence time of qubits^{18–21}. Secondly, the superconducting/spin correlation can only be changed by growing new samples with different composition or structural design. At the interface between inorganic and molecular materials, unique phenomena can emerge, such as surface states with distinct electrical and magnetic properties^{22–24}. Here, we show that these effects can be used to design carbon-based molecular hybrids, which can contribute to the design of superconducting spintronic devices without magnetic materials (Fig. 1a).

We study hybrid superconductor/molecule/normal metal (S/M/N) heterostructures using low-temperature electron transport to show that a C_{60} layer can mediate the leakage of Cooper pair states via the proximity effect. Systems that include a superconductor/molecule/spin-converter interface (S/M/ I_{S-C} /M/N) are characterised through a combination of transmission electron microscopy (TEM), polarised neutron and X-ray reflectivity (PNR/XRR). In addition, LE- μ SR is used to detect symmetry changes in superconducting pair correlations via a paramagnetic component to the Meissner screening. In

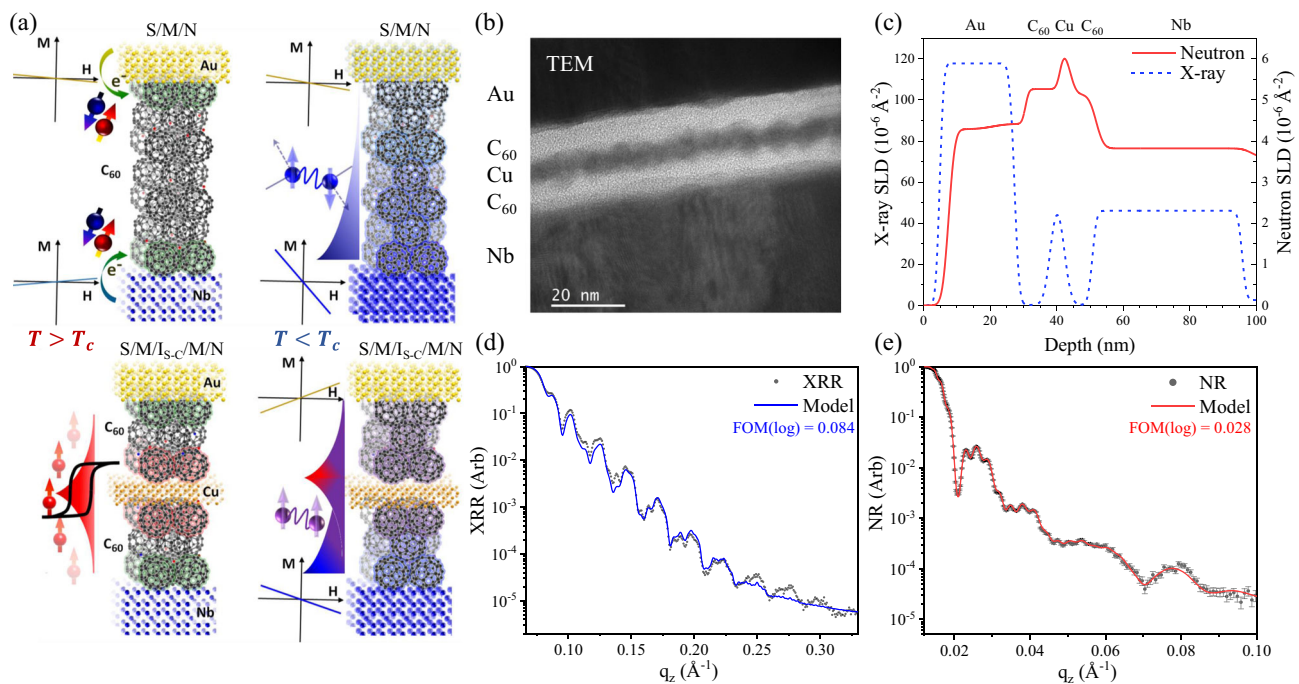


Fig. 1 Structural characterization of a prototypical superconductor/molecular heterostructure. The nominal structure is: $\text{SiO}_2/\text{Nb}(50)/\text{C}_{60}(10)/\text{Cu}(3)/\text{C}_{60}(10)/\text{Au}(20)$ where thicknesses in brackets are in nm. **a** A schematic demonstrating the proposed coalescence of localised interfacial spin-order and superconducting correlations in hybrid superconductor/molecule/normal metal (S/M/N) and superconductor/molecule/spin-converter interface (S/M/ I_{S-C} /M/N) heterostructures, above and below the superconducting transition temperature, T_c . **b** Transmission electron microscope (TEM) image of the S/M/ I_{S-C} /M/N sample where S, I_{S-C} and N layers are separated by continuous M layers aided by the minimal diffusion of sputtered Cu and Au. **c** The depth dependence of the fitted scattering length density (SLD) demonstrates the different sensitivities of neutron (continuous red line) and X-ray reflectivity (dashed blue line). By fitting the X-Ray reflectivity (**d**; grey points measurements, blue line model fit) and Neutron reflectivity (**e**; grey points measurements, red line model fit) with GenX, we confirm that the structural morphology is coherent over a larger in-plane length than is captured via TEM: In both instances, we display the logarithmic figure of merit generated by GenX.

the S/M/I_{S-C}/M/N system, the spin-converter interface layer refers to the spin-ordered state generated at the interface between C₆₀ and Cu²⁵. In all samples, the superconducting film is Nb, a conventional s-wave superconductor, with a T_c of ~9 K.

Results and discussion

Initial characterization. We performed structural characterisation on a prototypical S/M/I_{S-C}/M/N system with a nominal structure; S = Nb (50 nm), M = C₆₀(10 nm), I_{S-C} = Cu (3 nm) and N = Au (50 nm). The TEM image of the heterostructure shown in Fig. 1b demonstrates the resilience of the molecular layers to the diffusion of the metallic adatoms during the sputtering process. Energy-dispersive X-ray analysis confirms the complete separation of metallic layers by continuous C₆₀ barriers. Typically, XRR and PNR can be used to obtain structural parameters such as interfacial roughness (including interdiffusion), layer thickness and density –Fig. 1c. Given the relatively large X-ray scattering length density of Au, an XRR measurement of such a sample is dominated by the top Au layer, as shown in Fig. 1d. Low-angle neutron reflectivity shown in Fig. 1e aids the characterisation of layers buried within the heterostructure thanks to the smaller neutron scattering length density for Au. The reflectivity curves obtained by both techniques were fit using GenX to yield the parameters in Table 1 (ref. 26).

Low-temperature transport measurements. The use of thin-film C₆₀ based spin-polarised metallo-molecular interfaces for the creation of spin-triplet superconducting correlations requires that superconducting phase information can be carried across a molecular C₆₀ layer. Proximity-induced superconductivity of the molecular layer modifies the superconducting gap (Δ) at the interface of the Nb via the inverse proximity effect. Quantitatively, the reduction of Δ in the Nb layer due to a loss of Cooper pairs at the interface is indicated by a suppression of the superconducting transition temperature (T_c). This technique has been frequently used to study proximity effects in superconductor/normal metal bilayers for several decades²⁷. See supplementary Notes 1 and 2, Figs. S1–S3 and Table S1 for further detail on the sample structure and characterisation.

We grew two Nb films simultaneously on the same 8 × 8 mm² Si/SiO₂(100 nm) substrate, allowing the superconducting T_c of each S/M/N proximity stack to be normalised to that of control Nb films. C₆₀(t) and Au (20 nm) films were deposited onto one of the Nb films to create the S/M/N proximity stack where t = 0–80 nm. A 2-nm Al film was used to coat the whole substrate. This Al film passivates in atmosphere and protects the Nb from oxidation. A schematic of the sample chip featuring the S/M/N and control films is shown in Fig. 2a.

The S/M/N transition temperature has been normalised with respect to the Nb control film and is shown in Fig. 2b. The results

obtained are shown in blue for four different C₆₀ thicknesses (eight samples in total). We have assumed an exponential decay of the superconducting order parameter within the C₆₀ as is appropriate according to Ginzberg–Landau theory. From the fit, we extract an effective length scale for the propagation of Cooper pairs within the molecular layer of $\xi_{\text{Eff}} = 30 \pm 8$ nm. Measurements in a thin, discontinuous layer of C₆₀ islands²⁸ (t = 3.9 ± 0.1 nm) show almost no T_c suppression, Fig. 2b, c. For Andreev reflection at the Nb/C₆₀ interface to mediate a superconducting proximity effect, charge carriers in the C₆₀ layer must pair with electronic states in Nb through the retroreflection of a hole. Since T_c is not suppressed when the C₆₀ layer is discontinuous, a lower interface transparency must result from molecular islands that disrupt the Andreev reflection process. The leakage of Cooper pairs has been observed in single-molecule C₆₀²⁹, but the length scale over which the phase coherence decays had not been studied previously in thin films. Given a bandgap for bulk C₆₀ of 2.3 eV, it is perhaps surprising that Cooper pairs can propagate for 30 nm. However, the electronic properties of C₆₀ interfaced with metal surfaces are very different from the bulk, owing to charge transfer and molecular metallisation^{30–32}.

Low-energy muon spin spectroscopy in Single-Probe samples.

The leakage of Cooper pairs through a magnetic metal has been shown to lead to the generation of spin-polarised odd-frequency pairs^{33,34}. To determine the effect of a spin-converter molecular interface upon the superconducting order parameter pairing symmetry, we measure hybrid metallo-molecular systems with LE- μ SR. The technique can probe directly the Meissner state and the presence of spin-ordering as a function of depth within the sample. We fabricated and measured two sets of samples, which we refer to as ‘Single-Probe’ and ‘Multi-Probe’. For both sample sets, a comparison is made between structures with and without a Cu/C₆₀ spin-converter interface (I_{S-C}). The Single-Probe samples had nominal, bottom-up, structures of:

1. S/M/N : Nb(50)/C₆₀(20)/Au(50)
2. S/M/I_{S-C}/M/N : Nb(50)/C₆₀(10)/Cu(3)/C₆₀(10)/Au(50)

Thicknesses in brackets are in nm. The single 50-nm Au layer is used to moderate the muon beam. We include a 50-nm superconducting film so that the sample is in the mesoscopic regime for sputtered Nb; its thickness is greater than the superconducting coherence length, ($\xi \sim 10$ nm) while being less than the reported penetration depth ($\lambda_0 > 90$ nm)^{35,36}. This ensures that the contribution to the μ^+ precession signal from the conventional Meissner effect is minimised and no vortices can form in-plane. Because of a lack of electronic screening, muons stopping in the C₆₀ film will form muonium, a hydrogen-like bound state³⁷. In an applied transverse magnetic field (TF), the transitions between different spin configurations of the C₆₀ muonium state happen on a timescale that is shorter than the instrument resolution. Therefore, in this geometry we are only sensitive to the precession of the diamagnetic μ^+ particles stopping in the metallic layers.

The thicknesses of the C₆₀ layers have been engineered in all samples so that the separation between Au and Nb is shorter than, or equal to, the Cooper pair propagation length we measure in C₆₀ ($\xi_{\text{Eff}} \sim 30$ nm). The emergence of spin order at Cu/C₆₀ and its effect on the superconductor were probed first by magnetometry and low-temperature transport. The results are compared against the sample without the spin-converter interface. The onset of Meissner expulsion for the two samples occurs at very similar temperatures (Fig. 3a). However, the addition of the thin Cu layer leads to an emergent magnetic signal at RT due to

Table 1 Structural parameters obtained for the prototypical Nb/C₆₀/Cu/C₆₀/Au sample.

X-ray	Neutron			
	Layer	d[σ] (nm)	ρ (%)	d[σ] (nm)
Au	22.6 [1.0]	96.5	23.1 [1.5]	95.3
C ₆₀	10.3 [1.2]	99.2	10.5 [0.9]	95.7
Cu	4.5 [1.3]	95.6	2.9 [1.0]	95.5
C ₆₀	8.6 [1.3]	94.3	7.9 [1.5]	93.4
Nb	45.8 [1.1]	90.0	46.8 [1.8]	97.5

The X-ray and neutron reflectivity data have been modelled with GenX using the presented film thickness (d), rms roughness (σ) and density (ρ) of each layer. The density has been presented as a percentage w.r.t. the bulk.

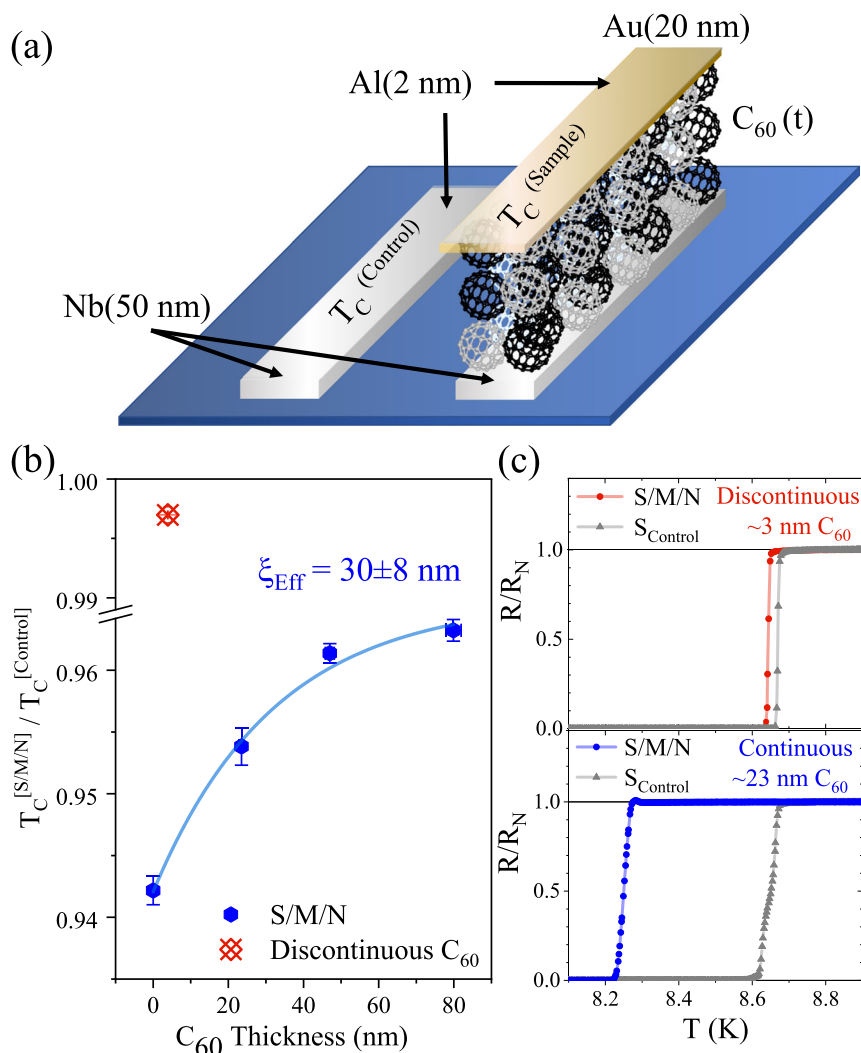


Fig. 2 Low-temperature characterisation of hybrid superconducting/molecular/metal heterostructures. **a** A schematic showing the fabricated sample which is grown alongside a control Nb film. **b** The dependence upon the superconducting transition temperature (T_c) suppression with C_{60} thickness for Nb (50 nm)/ $C_{60}(t)$ /Au(20 nm)/Al(2 nm) stacks for continuous (blue symbols) and discontinuous (red symbols) C_{60} films. The modification of the superconducting gap energy via the inverse proximity effect is greatest for the sample without C_{60} . As a fullerene barrier layer is introduced, and its thickness increased, the T_c never fully recovers to its pristine value. Therefore, there is a leakage of Cooper pair states into the C_{60} and through to the Au, where an effective length scale for the propagation of Cooper pairs is $\xi_{\text{Eff}} = 30 \pm 8$ nm. A y-axis line-break allows the data point obtained for the sample with a discontinuous island-like C_{60} barrier to be shown. Error bars are uncertainties in the critical temperature measurement. For each point, the T_c suppression is obtained via low-temperature transport measurements, such as those shown in **(c)**; grey symbols are for the control samples.

magnetic hardening (Fig. 3b)^{23,25,38}. The sample with the Cu/ C_{60} interface has a moment per area of $m = 27 \pm 1 \mu\text{emu cm}^{-2}$, which equates to a volume magnetisation of $90 \pm 3 \text{ emu cm}^{-3}$, assuming that the magnetic order is localised to the Cu. The sample without a Cu/ C_{60} interface has a moment of $m = 2 \pm 1 \mu\text{emu cm}^{-2}$, consistent with a typical instrumental background.

By fitting the temperature dependence of the out of plane critical field, $H_{c2\perp}(T)$, we obtain coherence lengths of $\xi_{\text{GL}} = 9.34 \pm 0.02$ (9.63 ± 0.02) nm for the sample without (with) the I_{S-C} , Fig. 3c. These values are typical for sputtered Nb in the dirty limit $l < \xi_0$, l being the electron mean free path^{39,40}. The muon implantation depth is dependent upon its energy, Fig. 3d. Once thermalised, it undergoes spin precession about the local field until decaying into a positron, emitted preferentially along the muon spin direction. Five million of these events are captured to fit the time evolution of the muon precession in a 300 G transverse field. The average magnetic flux for each implantation energy, $\langle B \rangle(E)$ is determined from the time-dependent polarisation of the muon,

and then we use the stopping profiles to obtain $\langle B \rangle(x)$ ^{41–43}, with $\langle x \rangle$ the average probing depth for each energy E .

$\langle B \rangle(x)$ is normalised to the average field within the superconductor in the normal state, B_N , and plotted against the average implantation depth. As a first approximation, we chose to model the flux expulsion entirely within the Nb layer. Although superconducting correlations reside within the proximitised C_{60} and Au layers, their relative screening amplitudes are expected to be weak and the signal dominated by the superfluid pair density in Nb. The $\langle B \rangle(x)$ profile for the non-magnetic Single-Probe sample can be accurately described by a London model with $\lambda(2.5 \text{ K}) = 218$ nm, in good agreement with sputtered Nb films in the dirty limit^{35,44}. However, when the spin-converter Cu/ C_{60} layer is in proximity to the Nb surface, the $\langle B \rangle(x)$ fit now yields $\lambda(2.5 \text{ K}) = 313$ nm, representing a sizeable modification to the superconducting properties of this system (Fig. 3e).

If there were a pair-breaking effect due to the exchange energy of the spin-ordered Cu/ C_{60} interface, then N_s for the spin-

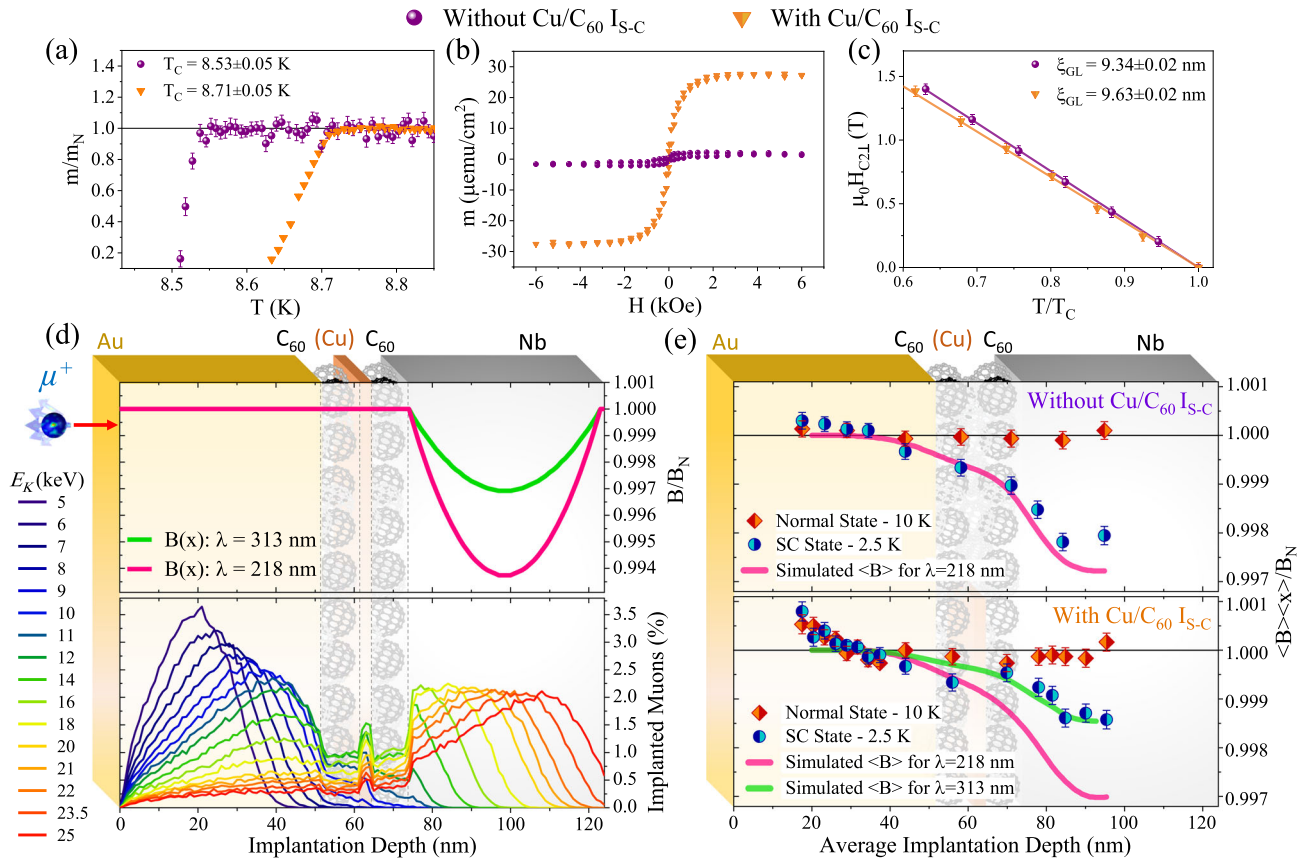


Fig. 3 Anomalous Meissner signal measured by low-energy muon spin rotation in Single-Probe samples. **a** Moment vs. temperature scans show that the onset of Meissner screening in the two samples occurs at similarly high temperatures (>8.5 K). **b** Magnetic hysteresis loops measured at 300 K, showing a moment of $27 \pm 1 \mu\text{emu}/\text{cm}^2$ (with Cu/C₆₀ interfaces; orange triangles) and $2 \pm 1 \mu\text{emu}/\text{cm}^2$ (without; purple dots). **c** The temperature dependence of the out of plane critical field, $H_{c2\perp}(T)$, for the two heterostructures gives similar Ginzberg-Landau coherence lengths. **d** Simulated magnetic flux profiles, $\langle B \rangle$, where the green and pink functions model the expected flux expulsion for London penetration lengths of 313 (green line) and 218 nm (pink line), respectively. The implantation distributions, according to the muon stopping depths for all energies used are also shown. **e** The average local magnetic flux, $\langle B \rangle$, measured at 2.5 K (orange diamonds) and 10 K (blue dots) and normalised to the flux density in the niobium layer at 10 K, B_N . The London model gives penetration lengths of 313 nm (with Cu/C₆₀) and 218 nm (without). Error bars are statistical variations over 5 million muon decay measurements.

converter sample would need to be roughly half that of the control S/M/N system to explain such an elongation of λ , since $\lambda^{-2} \propto N_s$. However, as demonstrated by the transport measurements in Fig. 3a, c, there is no suppression of superconductivity for the spin-converter sample. Instead, it has a slightly higher superconducting T_c . The reduced flux expulsion in the spin-converter interface may be the manifestation of an additional paramagnetic contribution quenching the diamagnetic Meissner effect.

Low-energy muon spin spectroscopy in Multi-Probe samples.

Ferromagnets may result in an enhanced Meissner expulsion due to changes in the boundary conditions or proximity effects driven by the vector potential^{45–47}. By contrast, the generation of odd-frequency spin-triplet pairing states at superconductor/ferromagnetic interfaces can suppress the conventional diamagnetic Meissner effect¹³. The supercurrent density, j , arising due to a magnetic vector potential, A , can be rewritten in terms of singlet (n_s) and triplet densities (n_t): $j \propto (n_s - n_t)$ ⁴⁸. Therefore, in a system where odd-frequency correlations exist, a paramagnetic susceptibility ($\chi > 0$) can develop locally if $n_t > n_s$ ^{14,15}. If the n_s/n_t ratio varies spatially throughout the spin-converter sample, then at some specific depths a paramagnetic signal might emerge where $n_s/n_t < 1$. In order to capture this contribution within $B(E)$ we use multiple thin Au probe layers that create deterministic stopping

locations for the muon particles, thus effectively increasing the depth resolution:

1. S/M/N : Nb(50)/C₆₀(30)/Au₁(10)/C₆₀(20)/Au₂(10)/C₆₀(20)/Au₃(10)
2. S/M/I_{S-C}/M/N : Nb(50)/C₆₀(15)/Cu(4)/C₆₀(15)/Au₁(10)/C₆₀(20)/Au₂(10)/C₆₀(20)/Au₃(10)

Transport measurements show excellent agreement between the two structures, with the T_c of both samples at ≥ 8.7 K – Fig. 4a. Supplementary Note 3 shows the optimisation of the local magnetic flux sensitivity, with the muon stopping profiles in Fig. S4. Hysteresis loops are shown in Fig. 4b, which demonstrates that the sample with the I_{S-C} has a moment per area, $m = 24 \pm 1 \mu\text{emu}/\text{cm}^2$ – very similar to that measured in the previous set. The sample without Cu shows a background signal of $m = 0.4 \pm 0.2 \mu\text{emu}/\text{cm}^2$.

Muon measurements were performed at 9 and 20 keV to probe local screening effects at the Au layer closest to the superconductor (Au₁) and within the Nb layer, respectively, see Fig. 4c, e. At 9 keV, the highest fraction of thermalised μ^+ particles (x_{max}) in both control and spin-converter samples lies within the Au₁ layer, with no muons stopping in the Nb. Therefore, we can decouple the signal arising from screening currents within the Au₁ probe layer from the superconducting substrate. At 20 keV, x_{max} lies 10–20 nm inside the Nb layer, and there is only a small contribution to the signal from the Au layers. See the Supplementary Notes 3 and 5 for

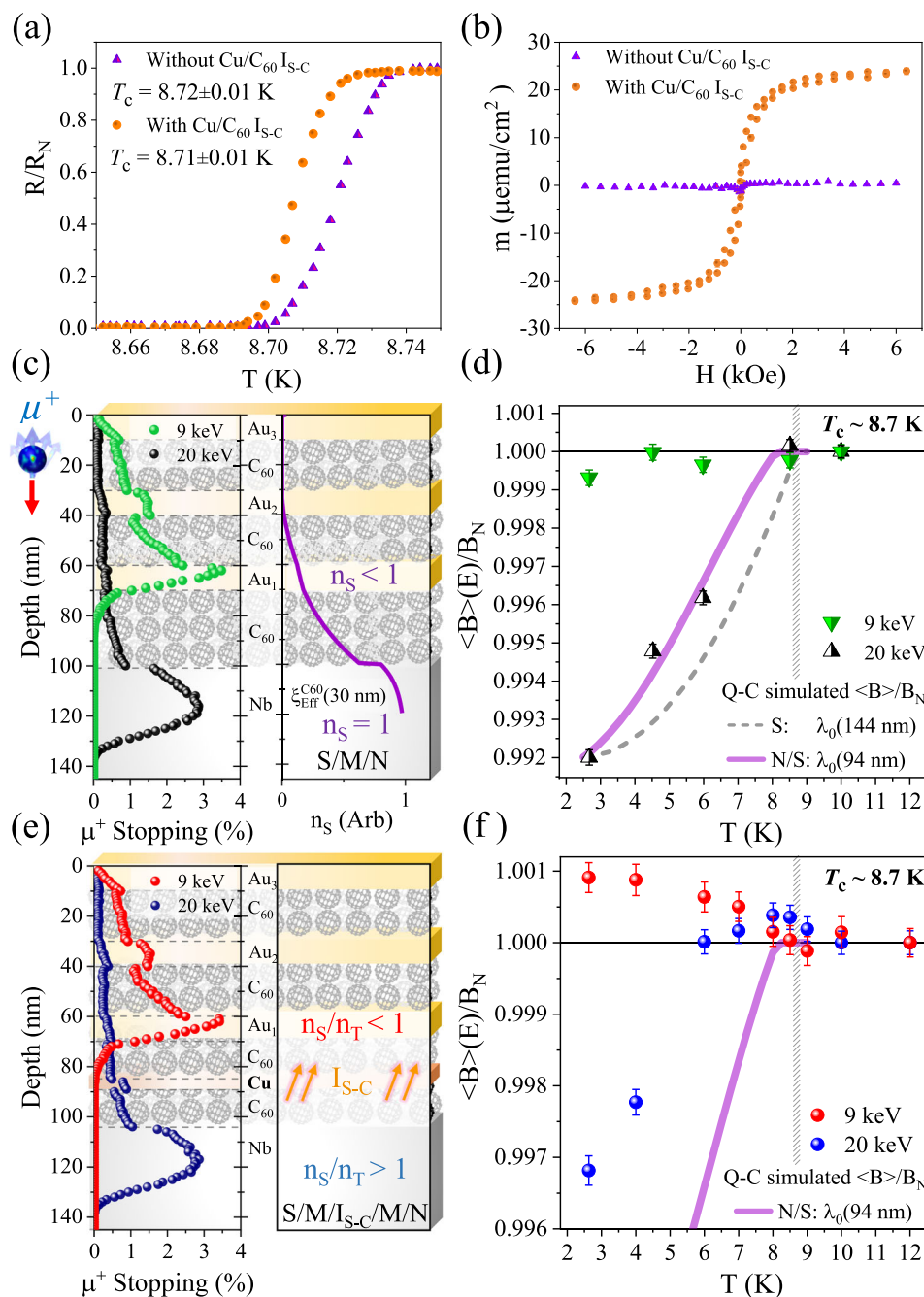


Fig. 4 Low-energy muon spin rotation measurements of screening effects in Multi-Probe hybrid proximity stacks. **a** The two samples have very similar superconducting transition temperatures (T_c). **b** Magnetic hysteresis loops at 300 K for the two Multi-Probe sister samples. The saturation magnetisation per unit area are $24 \pm 1 \mu\text{emu cm}^{-2}$ (with Cu/C_{60} ; orange dots) and $0.4 \pm 0.2 \mu\text{emu cm}^{-2}$ (without; purple triangles). **c** Simulated stopping profiles for the superconductor/molecular/normal metal (S/M/N) structure at 9 keV (green symbols) and 20 keV (black symbols). At 9 keV, no muons are implanted into the Nb film; this is also true for the superconductor/molecular/spin-converter interface (S/M/I_{S-C}/M/N) structure in **e**. **d** Temperature dependence of the average local field, $\langle B \rangle(E)$, in a 300 G applied transverse field for the S/M/N structure. Well below T_c , a small reduction in $\langle B \rangle(E)$ is observed in the Au layer at 9 keV implantation energy. This small Meissner screening originates from the leakage of Cooper pair states through the C_{60} and into the Au layer. At 20 keV, muons stop exclusively in the Nb layer, and a large conventional Meissner effect is observed. **e** Simulated stopping profiles at 9 keV (red symbols) and 20 keV (blue symbols) show that the depth dependence of the muon implantation is mostly unaffected by the inclusion of the spin-converter layer. **f** The temperature dependence of the measured local field in a 300 G applied transverse field for the S/M/I_{S-C}/M/N structure. Below T_c , an increase in B is observed in the Au layer at 9 keV (red symbols) due to the presence of odd-parity pairs. At 20 keV (blue symbols), the conventional Meissner effect is roughly half compared to the sample without the spin-converter Cu/C_{60} interface. Error bars are statistical variations over 5 million muon decay measurements.

further detail and comparisons between single and multi-probe structures.

The temperature dependence of $\langle B(E) \rangle / B_N$ for the sample without the spin-converter Cu/C₆₀ interface is shown in Fig. 4d. There is a reduction in the internal field arising from the conventional Meissner effect as the sample is cooled through the critical temperature. For muons probing the Nb layer (20 keV), the Meissner effect results in a 2.41 ± 0.08 G reduction of the internal field going from 10 K to 2.7 K. When probing the Au layer at 9 keV, the internal field at 2.7 K shows a 0.21 ± 0.08 G reduction, consistent with the presence of even-frequency superconducting correlations in this region. See Supplementary Note 3 for the depolarisation dependence of the LE- μ SR vs. temperature (Fig. S5).

We can simulate the $\langle B \rangle(T)$ data at 20 keV using a quasi-classical (Q-C) framework. Here, spin-singlet superconducting correlations are described by Green functions. In the dirty limit, these Green functions satisfy the Usadel equation^{45,49}. Within this framework, interfacial boundary conditions are imposed between the normal conductor (N) and superconductor (S) layer⁵⁰. Once the Green functions are determined, we apply the linear response theory to calculate the screening current (and thus $\langle B \rangle(T)$) in response to small externally applied field – see Supplementary Note 5. The density of states of the Nb layer, tuned to achieve the flux expulsion measured at the lowest temperature, equates to a λ_0 of 144 nm (S model). However, this simple model cannot replicate the $B/B_N(T)$ trend in the S/M/N system. Instead, we assume that the suppressed T_c observed in Fig. 2 is due to proximity-induced superconductivity in the C₆₀ layer, this reduces the order parameter, Δ , toward the Nb/C₆₀ interface. We find then a density of states equating to a λ_0 of 94 nm and a near-linear $B(T)$ trend that fits well the experimental data – see Fig. 4d.

Figure 4f shows the temperature dependence of $\langle B(E) \rangle / B_N$ for the sample with the spin-converter Cu/C₆₀ interface. The reduction in the local field in the Nb film at 20 keV is less than half of what was observed in the control: 1 ± 0.1 G at 2.7 K. The 9 keV measurements probing the Au layer now show a paramagnetic signal of 0.3 ± 0.1 G at 2.7 K. This sample also shows an anomalous temperature dependence of the Meissner effect, very different to the Q-C calculations. The Supplementary Note 5 explains further the Q-C simulation of the flux expulsion in Nb/C₆₀/Au structures, see Fig. S6. The T_c of this sample is comparable to the control sample without Cu ($T_c \sim 8.7$ K), but there is not an immediate reduction in the local field below T_c as would be expected. Instead, $\langle B(E) \rangle$ in Nb (20 keV) is only reduced w.r.t. the normal state once the sample is below 6 K ($\sim 0.7 T_c$). The conversion of even-frequency superconducting correlations into odd-frequency correlations at the spin-converter Cu/C₆₀ interface has given rise to a suppressed diamagnetic Meissner response in the niobium layer and a paramagnetic supercurrent in the Au layer, consistent with a majority odd-frequency pair density residing in this region of the heterostructure^{51–55}.

A paramagnetic signal may arise due to other phenomena, such as instabilities brought about by π -states formed at superconductor/non-magnetic interfaces or inhomogeneities in the superconductor lattice^{56,57}. Locally pinned flux in mesoscopic superconducting systems has produced an observable paramagnetic screening signal due to sample morphology^{58–60}. In our experiments, our range of control samples rules out these paramagnetic contributions, as all samples share the same superconductor/molecular interface with consistent morphologies confirmed by XRR and TEM. Moreover, pinned flux or orbital paramagnetism in the near-surface region of the Nb layer would lead to a broadening of the field distribution below T_c .

Should these phenomena be prevalent in our systems, we would expect a significant increase in the muon depolarisation rate below T_c for the spin-converter sample. As can be seen in the Supplementary Notes 3 and 5, this is not the case. Additionally, our choice of a 300 G transverse field should sufficiently quench the orbital paramagnetism possible at superconductor/non-magnetic interfaces⁶¹. Rather, the paramagnetic screening we observe that is concentrated in the Au layer is most likely the result of triplet correlations extending into this layer. Supplementary Note 6 and Fig. S7 show the field dependence of the spin susceptibility at 120 G and 300 G for different muon energies in the multi-probe sample.

Conclusions

The results presented here demonstrate that in thin-film form, superconducting correlations can be mediated across a molecular C₆₀ layer of sufficiently small thickness. We suggest that changes to the C₆₀ electronic structure, brought about by interfacial hybridisation and charge transfer, may allow for this proximity to manifest. With the addition of a spin-converter metallo-molecular interface, a reproducible paramagnetic screening response was observed by LE- μ SR due to the conversion of spin-singlet Cooper pairs to of odd-frequency spin-triplet states at the magnetic Cu/C₆₀ interface. The anomalous response of the sample flux profile in the superconducting state to both temperature and magnetic field provides a compelling case for the presence of unconventional superconducting states present in a hybrid metal/molecule superconducting system. A spin-selective ferromagnetic layer could be used in conjunction with the spin converter interface to generate the $S_Z = 1$ long-range spin-triplet. The triplet filtering can be used for super-spintronics or in coherence and interferometry applications^{62,63}. Given that the metallo-molecular interface charge transfer and interactions can be controlled via electrical or optical irradiation, this opens further avenues of research to produce, switch and control odd-frequency superconducting correlations for quantum computing in an intrinsically non-magnetic and non-superconducting system.

Methods

Thin film growth and characterisation. Metallic films were grown by DC magnetron sputtering, while C₆₀ molecular films were thermally sublimed in situ at 450 °C. Deposition of all sample layers was performed under UHV with a base pressure of 10^{-8} Torr and partial pressure of oxygen of 10^{-10} Torr. Sputtering was performed in an Ar atmosphere at 2.4 Torr from targets with purities of Nb (99.9999%), Cu(99.99999%) and Au(99.99%). Growing the heterostructure in this way leads to nanocrystalline C₆₀ layers and polycrystalline metallic films⁶⁴. The growth rate for these materials was calibrated by the fitting of Kiessig fringes measured by XRR. The NR data was obtained using the PolRef beamline at the ISIS Neutron and Muon Source, UK⁶⁵.

Low-energy muon spin rotation analysis. For this study, two sets of samples were fabricated and measured on the μ E4 beamline at the Paul Scherrer Institute, Switzerland⁶⁶. Characterisation measurements were performed on ‘sister samples’ grown at the same time as the LEM samples but on 4×4 mm² substrates, suitable for the SQUID VSM, and low-temperature measurements. The Ginzburg-Landau (GL) coherence length at 0 K, ξ_{GL} , for the Single-Probe samples, was extracted using the following relationship;

$$\mu_0 H_{C2\perp}(T) = \left(\frac{\phi_0}{2\pi\xi_{GL}^2} \right) \left(1 - \frac{T}{T_c} \right) \quad (1)$$

where ϕ_0 is the flux quantum and $H_{C2\perp}(T)$ is the out of plane critical field.

Samples used for LEM measurements are grown on 20×20 mm² substrates which reduces the associated count time. The time-dependent polarisation ($P(t)$) of the muon can be described by

$$P(t) = A_{\mu^+} \cos(\gamma_{\mu^+} \langle B \rangle(E) \cdot t + \varphi) \exp(-\lambda_{TF} \cdot t) \quad (2)$$

to yield the local field $\langle B \rangle(E)$, depolarisation rate (λ_{TF}), asymmetry (A_{μ^+}) and phase (φ). γ_{μ^+} is the gyromagnetic ratio of the muon. φ is the starting phase of the μ^+ spin

polarisation at time $t = 0$; this initial μ^+ spin polarisation depends on the time of flight of the muon in the fringe field of the magnet, which in turn depends on the implantation energy. A_{μ^+} will also be energy-dependent as it parametrises the magnitude of the μ^+ precession signal. For implantation energies where a more significant proportion of the muons thermalise within C_{60} , a reduction in A_{μ^+} would be expected due to the formation of muonium. As both parameters are verified to be independent of temperature, they can be fixed at the value obtained in the normal state for each implantation energy. Therefore, only $\langle B \rangle(E)$ and λ_{TF} are affected by the onset of screening currents within the heterostructure.

Following on from the London equation, the expected flux profile $B(x)$ within the superconductor is given by

$$B(x) = B_N \cosh\left(\frac{x}{\lambda(T)} - \frac{d_s}{2\lambda(T)}\right) \cosh\left(\frac{d_s}{2\lambda(T)}\right)^{-1} \quad (3)$$

where x is the position within the superconducting film, $x = 0$ corresponds to the top surface of the Nb layer. d_s is the Nb thickness. $\lambda(T)$ is the temperature-dependent penetration depth and B_N is the flux outside the superconductor, which in this case, has been obtained from the normal state measurement at 10 K⁴⁵. All data presented is publically available⁶⁷.

Data availability

The data that support the findings of this study are available from <https://doi.org/10.5518/852>. The neutron reflectivity data are available from <https://doi.org/10.5286/ISIS.ERB1820617>.

Received: 22 October 2020; Accepted: 1 March 2021;

Published online: 08 April 2021

References

- Coronado, E. et al. Coexistence of superconductivity and magnetism by chemical design. *Nat. Chem.* **2**, 1031–1036 (2010).
- Serrano, G. et al. Quantum dynamics of a single molecule magnet on superconducting Pb(111). *Nat. Mater.* **19**, 546–551 (2020).
- Alpern, H. et al. Unconventional superconductivity induced in Nb films by adsorbed chiral molecules. *New J. Phys.* **18**, 113048 (2016).
- Shapira, T. et al. Unconventional order parameter induced by helical chiral molecules adsorbed on a metal proximity coupled to a superconductor. *Phys. Rev. B* **98**, 214513 (2018).
- Bergeret, F. S., Volkov, A. F. & Efetov, K. B. Long-range proximity effects in superconductor ferromagnet structures. *Phys. Rev. Lett.* **86**, 4096–4099 (2001).
- Eschrig, M., Kopu, J., Cuevas, J. C. & Schön, G. Theory of half-metal/superconductor heterostructures. *Phys. Rev. Lett.* **90**, 137003 (2003).
- Linder, J. & Robinson, J. W. Superconducting spintronics. *Nat. Phys.* **11**, 307–315 (2015).
- M. Eschrig, Spin-polarized supercurrents for spintronics: a review of current progress. *Rep. Prog. Phys.* **78**, 104501 (2015).
- J Linder, AV Balatsky, Odd-frequency superconductivity. *Rev. Mod. Phys.* **91**, 45005 (2019).
- Leksins, P. V. et al. Evidence for triplet superconductivity in a superconductor-ferromagnet spin valve. *Phys. Rev. Lett.* **109**, 057005 (2012).
- N Banerjee, et al. Evidence for spin selectivity of triplet pairs in superconducting spin valves. *Nat. Commun.* **5**, 3048 (2014).
- Diesch, S. et al. Creation of equal-spin triplet superconductivity at the Al/EuS interface. *Nat. Commun.* **9**, 1–8 (2018).
- T, Yokoyama, Y, Tanaka, N, Nagaosa. Anomalous Meissner effect in a normal-metal superconductor junction with a spin-active interface. *Phys. Rev. Lett.* **106**, 246601 (2011).
- M, Alidoust, K, Halterman, J, Linder. Meissner effect probing of odd-frequency triplet pairing in superconducting spin valves. *Phys. Rev. B* **89**, 54508 (2014).
- A, Di Bernardo, et al. Intrinsic paramagnetic meissner effect due to s-wave odd-frequency superconductivity. *Phys. Rev. X* **5**, 41021 (2015).
- T, Champel, M, Eschrig. Effect of an inhomogeneous exchange field on the proximity effect in disordered superconductor-ferromagnet hybrid structures. *Phys. Rev. B* **72**, 54523 (2005).
- T. S., Khaire, M. A., Khasawneh, W. P., Pratt, N. O., Birge. Observation of spin-triplet superconductivity in co-based josephson junctions. *Phys. Rev. Lett.* **104**, 137002 (2010).
- Tahan, C., Friesen, M. & Joynt, R. Decoherence of electron spin qubits in Si-based quantum computers. *Phys. Rev. B* **66**, 1–11 (2002).
- Bergli, J., Galperin, Y. M. & Altshuler, B. L. Decoherence in qubits due to low-frequency noise. *New J. Phys.* **11**, 25002 (2009).
- Zwanenburg, F. A. et al. Silicon quantum electronics. *Rev. Mod. Phys.* **85**, 961–1019 (2013).
- Devoret, M. H. & Schoelkopf, R. J. Superconducting circuits for quantum information: an outlook. *Science* **339**, 1169–1174 (2013).
- Alves, H., Molinari, A. S., Xie, H. & Morpurgo, A. F. Metallic conduction at organic charge-transfer interfaces. *Nat. Mater.* **7**, 574–580 (2008).
- Al Ma'Mari, F. et al. Emergent magnetism at transition-metal-nanocarbon interfaces. *Proc. Natl Acad. Sci. USA* **114**, 5583–5588 (2017).
- Cinchetti, M., Dediu, V. A. & Hueso, L. E. Activating the molecular spininterface. *Nat. Mater.* **16**, 507–515 (2017).
- Al Ma'Mari, F. et al. Beating the Stoner criterion using molecular interfaces. *Nature* **524**, 69–74 (2015).
- Björck, M. & Andersson, G. GenX: an extensible X-ray reflectivity refinement program utilising differential evolution. *J. Appl. Crystallogr.* **40**, 1174–1178 (2007).
- Clarke, J. The proximity effect between superconducting and normal thin films in zero field. *J. Phys. Colloq.* **29**, C2–3–C2–16 (1968).
- Bommel, S. et al. Unravelling the multilayer growth of the fullerene C60 in real time. *Nat. Commun.* **5**, 5388 (2014).
- Winkelmann, C. B., Roch, N., Wernsdorfer, W., Bouchiat, V. & Balestro, F. Superconductivity in a single C60 transistor. *Nat. Phys.* **5**, 876–879 (2009).
- Haddon, R. C. et al. C60 thin film transistors. *Appl. Phys. Lett.* **67**, 121–123 (1995).
- Niederhausen, J. et al. Doping of C60 (sub)monolayers by Fermi-level pinning induced electron transfer. *Phys. Rev. B* **86**, 1–5 (2012).
- Maxwell, A. J., Brühwiler, P. A., Nilsson, A., Mårtensson, N. & Rudolf, P. Photoemission, autoionisation, and x-ray-absorption spectroscopy of ultrathin-film C60 on Au(110). *Phys. Rev. B* **49**, 10717–10725 (1994).
- J, Linder, T, Yokoyama, A, Sudbø, M, Eschrig. Pairing symmetry conversion by spin-active interfaces in magnetic normal-metal-superconductor junctions. *Phys. Rev. Lett.* **102** (2009).
- J, Linder, A, Sudbø, T, Yokoyama, R, Grein, M, Eschrig. Signature of odd-frequency pairing correlations induced by a magnetic interface. *Phys. Rev. B* **81** (2010).
- A. I., Gubin, K. S., Il'in, S. A., Vitusevich, M. Siegel, & N. Klein, Dependence of magnetic penetration depth on the thickness of superconducting Nb thin films. *Phys. Rev. B* **72**, 64503 (2005).
- Flokstra, M. G. et al. Measurement of the spatial extent of inverse proximity in a Py/Nb/Py superconducting trilayer using low-energy muon-spin rotation. *Phys. Rev. B* **89**, 54510 (2014).
- Kiefl, R. F. et al. Evidence for endohedral muonium in Kx C60 and consequences for electronic structure. *Phys. Rev. Lett.* **69**, 2005–2008 (1992).
- Martín-Olivera, L., Shchukin, D. G. & Teobaldi, G. Role of metal lattice expansion and molecular p-conjugation for the magnetic hardening at Cu-organics interfaces. *J. Phys. Chem. C* **121**, 23777–23787 (2017).
- Schöck, M., Sürgers, C. & Löhneysen, H. V. Superconducting and magnetic properties of Nb/Pd_{1-x}Fe_x/Nb triple layers. *Eur. Phys. J. B* **14**, 1–10 (2000).
- Cirillo, C. et al. Long-range proximity effect in Nb-based heterostructures induced by a magnetically inhomogeneous permalloy layer. *N. J. Phys.* **19**, 23037–23037 (2017).
- Morenzoni, E. et al. Implantation studies of keV positive muons in thin metallic layers. *Nucl. Instrum. Methods Phys. Res. Sect. B Beam Interact. Mater. At.* **192**, 254–266 (2002).
- Suter, A. & Wojek, B. M. Musfit: a free platform-independent framework for μ sR data analysis. *Phys. Procedia* **30**, 69–73 (2012).
- Flokstra, M. G. et al. Remotely induced magnetism in a normal metal using a superconducting spin-valve. *Nat. Phys.* **12**, 57–61 (2015).
- Zhang, H. et al. Measurements of magnetic screening lengths in superconducting Nb thin films by polarised neutron reflectometry. *Phys. Rev. B* **52**, 10395–10404 (1995).
- M. G., Flokstra, et al., Observation of Anomalous Meissner Screening in Cu/Nb and Cu/Nb/Co Thin Films. *Phys. Rev. Lett.* **120**, 247001 (2018).
- Mironov, S., Mel'nikov, A. S. & Buzdin, A. Electromagnetic proximity effect in planar superconductor-ferromagnet structures. *Appl. Phys. Lett.* **113**, 22601 (2018).
- R., Stewart, et al. Controlling the electromagnetic proximity effect by tuning the mixing between superconducting and ferromagnetic order. *Phys. Rev. B* **100**, 20505 (2019).
- S., Mironov, A., Mel'Nikov, & A., Buzdin. Vanishing meissner effect as a hallmark of in-plane fulde-ferrell-larkin- ovchinnikov instability in superconductor-ferromagnet layered systems. *Phys. Rev. Lett.* **109**, 237002 (2012).
- Usadel, K. D. Generalised diffusion equation for superconducting alloys. *Phys. Rev. Lett.* **25**, 507–509 (1970).
- Nazarov, Y. V. Novel circuit theory of Andreev reflection. *Superlattices Microstruct.* **25**, 1221–1231 (1999).
- Walter, H. et al. Low-temperature anomaly in the penetration depth of YBa2Cu3O7 films: Evidence for Andreev bound states at surfaces. *Phys. Rev. Lett.* **80**, 3598–3601 (1998).

52. Asano, Y. et al. Unconventional surface impedance of a normal-metal film covering a spin-triplet superconductor due to odd-frequency cooper pairs. *Phys. Rev. Lett.* **107**, 087001 (2011).
53. Suzuki, S. I. & Asano, Y. Paramagnetic instability of small topological superconductors. *Phys. Rev. B Condens. Matter Mater. Phys.* **89**, 184508 (2014).
54. Espedal, C., Yokoyama, T. & Linder, J. Anisotropic paramagnetic meissner effect by spin-orbit coupling. *Phys. Rev. Lett.* **116**, 127002 (2016).
55. Krieger, J. A. et al. Proximity-induced odd-frequency superconductivity in a topological insulator. *Phys. Rev. Lett.* **125**, 026802 (2020).
56. S., Aull, O., Kugeler, & J., Knobloch. Trapped magnetic flux in superconducting niobium samples. *Phys. Rev. Special Topics Accel. Beams* **15**, 62001 (2012).
57. Fauchère, A. L., Belzig, W. & Blatter, G. Paramagnetic instability at normal-metal-superconductor interfaces. *Phys. Rev. Lett.* **82**, 3336–3339 (1999).
58. Geim, A. K. et al. Paramagnetic Meissner effect in small superconductors. *Nature* **396**, 144–146 (1998).
59. Braunisch, W. et al. Paramagnetic Meissner effect in Bi high-temperature superconductors. *Phys. Rev. Lett.* **68**, 1908–1911 (1992).
60. Thompson, D. J. et al. Observation of paramagnetic Meissner effect in niobium disks. *Phys. Rev. Lett.* **75**, 529–532 (1995).
61. Bruder, C. & Imry, Y. Orbital paramagnetism of electrons in proximity to a superconductor. *Phys. Rev. Lett.* **80**, 5782 (1998).
62. Giovannetti, V. & Yuasa, K. Probing Cooper pairs with Franson interferometry. *Phys. Rev. B* **86**, 115429 (2012).
63. Hofstetter, L., Csonka, S., Nygård, J. & Schönenberger, C. Cooper pair splitter realized in a two-quantum-dot Y-junction. *Nature* **461**, 960–963 (2009).
64. Shoup, J. E. et al. Structural studies of magnetic C60/Cu multilayers. *AIP Adv.* **10**, 025312 (2020).
65. Webster, J. R., Langridge, S., Dalgliesh, R. M. & Charlton, T. R. Reflectometry techniques on the second target station at ISIS: Methods and science. *Eur. Phys. J.* **126**, 1–5 (2011).
66. Prokscha, T. et al. The new mE4 beam at PSI: A hybrid-type large acceptance channel for the generation of a high intensity surface-muon beam. *Nucl. Instrum. Methods Phys. Res. Sect. A Accel. Spectrom. Detect. Assoc. Equip.* **595**, 317–331 (2008).
67. Rogers, M. et al. *Data on Spin-singlet to Triplet Cooper Pair Converter Interface* <https://doi.org/10.5518/852> (2020).

Acknowledgements

This work was supported by EPSRC grant nos. EP/S030263/1, EP/M000923/1 and EP/K00512X/1. Experiments performed at the ISIS Pulsed Neutron and Muon Source were supported by a beamtime allocation from the Science and Technology Facilities Council

experiment number RB 1820617. PSI LEM beamtime access via proposal IDs 20161840, 20171184 and 20190352.

Author contributions

M.R. fabricated the samples, carried out transport, X-ray and neutron reflectivity, magnetometry and LE- μ SR measurements and wrote the manuscript. A.W. grew samples and performed TEM measurements with the aid of the Leeds Electron Microscopy and Spectroscopy Centre. F.A.M., M.G.F., S.Lee, R.S., H.B. and T.P. contributed to the LE- μ SR measurements and analysis. A.J.C., C.J.K and S.Langridge contributed to the neutron reflectivity measurements and analysis. T.M., M.A., G.B. and B.J.H. contributed toward the sample design, instrumentation and data analysis. O.C. was responsible for the project planning, contributed to the experimental work, supervised and managed the work.

Competing interests

The authors declare no competing interests.

Additional information

Supplementary information The online version contains supplementary material available at <https://doi.org/10.1038/s42005-021-00567-7>.

Correspondence and requests for materials should be addressed to M.R. or O.C.

Reprints and permission information is available at <http://www.nature.com/reprints>

Publisher's note Springer Nature remains neutral with regard to jurisdictional claims in published maps and institutional affiliations.



Open Access This article is licensed under a Creative Commons Attribution 4.0 International License, which permits use, sharing, adaptation, distribution and reproduction in any medium or format, as long as you give appropriate credit to the original author(s) and the source, provide a link to the Creative Commons license, and indicate if changes were made. The images or other third party material in this article are included in the article's Creative Commons license, unless indicated otherwise in a credit line to the material. If material is not included in the article's Creative Commons license and your intended use is not permitted by statutory regulation or exceeds the permitted use, you will need to obtain permission directly from the copyright holder. To view a copy of this license, visit <http://creativecommons.org/licenses/by/4.0/>.

© The Author(s) 2021